

Supporting Information

Trifunctional GdCoO₃ Perovskite Electrocatalysts for Zinc-Air Battery and Water Electrolysis Applications

Annet Anna Thomas,^{†[a](#)} Anook Nazer Eledath,^{†[b](#)} M. Junaid Bushiri^a and Azhagumuthu Muthukrishnan ^{*,[b](#)}

No.	Contents	Page(s)
1	Materials, ECSA and TOF calculations	S2
2	<u>Characterisation:</u> PXRD, TGA and corresponding PXRD, SEM, SEM-Elemental mapping, HR-TEM images, BET isotherm, Pore size distribution analysis, XPS survey spectra, individual deconvoluted spectra	S3- S16
3	<u>Electrochemical analysis:</u> RRDE and RDE voltammograms, OER activity and Tafel slopes for control samples, HER activity and Tafel slopes for control samples	S17- S24
4	<u>Zinc air battery Performance:</u> liquid and solid-state zinc air battery polarisation curves, charge-discharge, and post-mortem analysis	S25-S30
5	<u>Tables:</u> Characterisation of materials	S31-S34
	Electrochemical analysis of ORR, OER, and HER	S35-S39
	Zinc air battery performance comparison	S40
6	References	S41

Chemicals used

Gadolinium nitrate hexahydrate ($\text{Gd}(\text{NO}_3)_3 \cdot 6\text{H}_2\text{O}$) was purchased from SRL, India. Cobalt nitrate hexahydrate ($\text{Co}(\text{NO}_3)_3 \cdot 6\text{H}_2\text{O}$), from Avra Chemicals, citric acid ($\text{C}_6\text{H}_8\text{O}_7$) was purchased from Merck, India, and Ketjen black (EC 300 J) was received from Lions Specialty Chemicals Co. Ltd, Japan. All the chemicals were of analytical grade and used as received.

Electrochemical surface area

The electrochemical active surface area (ECSA) and the double layer capacitance (C_{dl}) is recorded by taking the CV in the non-Faradaic region from 1 to 1.1 V vs. RHE at different scan rates of 10, 20, 30, 40, 50 mV/s. The CV recorded for all the compounds at different scan rate is given below. C_{dl} is determined from the slope of graph drawn with average current vs the scan rate. The calculated C_{dl} value and ECSA for all the compounds is given in the Table R1.

$$\text{ECSA} = \frac{C_{dl}}{C_s}$$

Where, C_{dl} is double-layer capacitance of the system, which is taken as the slope of the linear fits to the graph plotted with current (average of cathodic and anodic charging currents measured at 1.05 V vs RHE) as a function of scan rate. C_s is the specific capacitance of electrode; a typical value of 0.04 mF cm^{-2} is taken in alkaline solutions.

TOF calculation

Turn over frequency (TOF): The TOF of the materials are calculated as previously reported procedure based on the following formula (*Advanced Materials* **2024**, *36* (18), 2310938)

$$TOF = \frac{I \times N_A}{n \times F \times \tau}$$

Where I is the current at a fixed potential, N_A is the Avogadro number, and n is the number of electrons transferred (n is taken as 2 for HER and 4 for OER), F is the Faraday constant (96485 C mol^{-1}) and τ is the number of active sites involved in the reaction, which can be calculated using the following relation.

$$\tau = \frac{\text{area of CV curve}}{\text{scan rate} \times 1.601 \times 10^{-19}}$$

The C_{dl} was obtained by taking CV at various scan rates of non-faradaic region of the voltammogram.

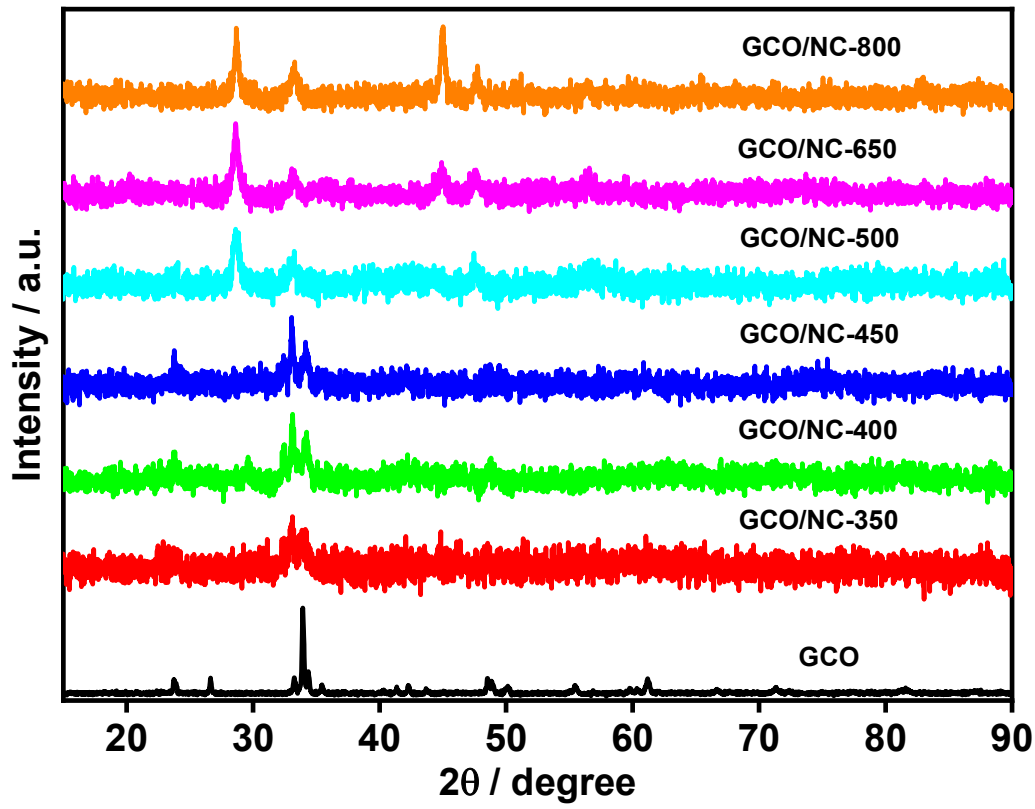


Figure S1. XRD patterns of GCO/NC at different pyrolysis temperatures (350, 400, 450, 500, 650, and 800 °C) in N₂ atmosphere.

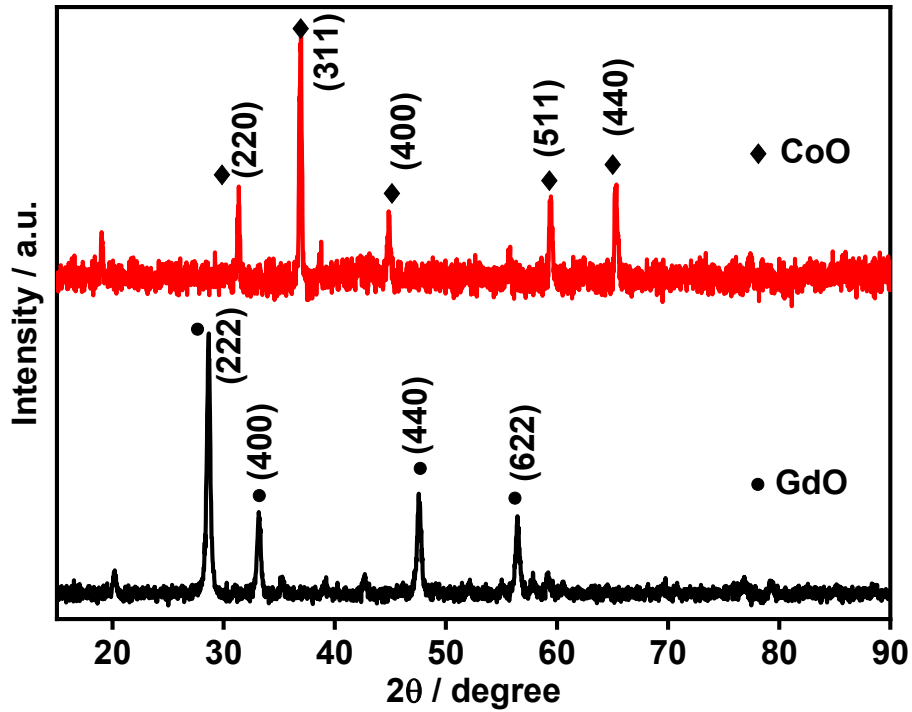


Figure S2. Power X-ray diffraction patterns of Gd_2O_3 and Co_3O_4

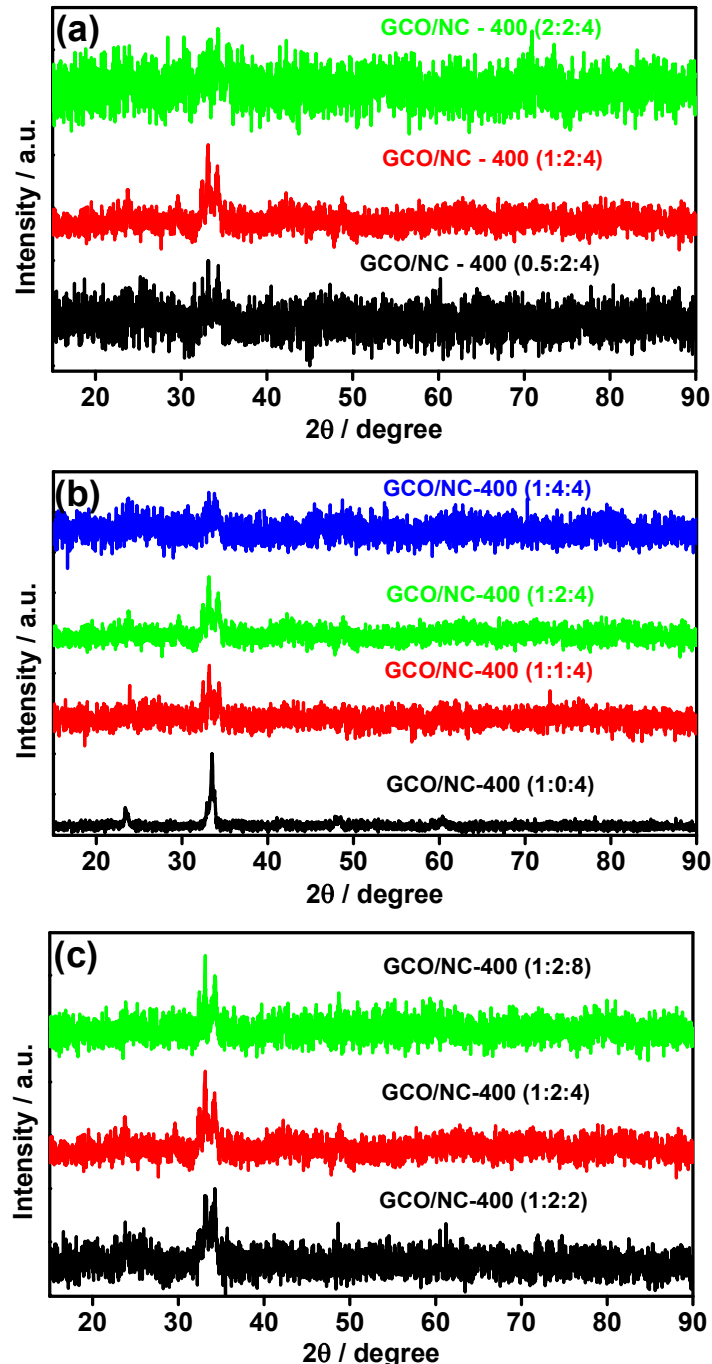


Figure S3. XRD pattern of composites by varying the (a) amount of GCO in the samples, namely GCO/NC-400 (0.5:2:4), GCO/NC-400 (1:2:4), GCO/NC-400 (2:2:4), (b) amount of KB in the samples, namely GCO/NC-400 (1:0:4), GCO/NC-400 (1:1:4), GCO/NC-400 (1:2:4) and GCO/NC-400 (1:4:4), and (c) amount of urea in the samples, namely GCO/NC-400 (1:2:2), GCO/NC-400 (1:2:4), GCO/NC-400 (1:2:8).

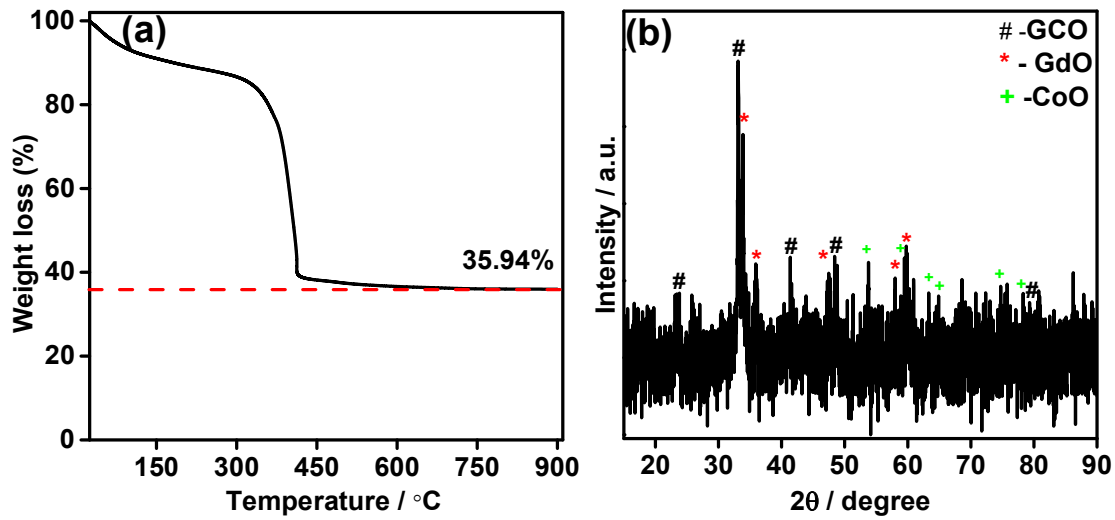


Figure S4. (a) Thermogravimetric analysis of GCO/NC-400 composite in air atmosphere and (b) the powder XRD pattern of the remaining sample.

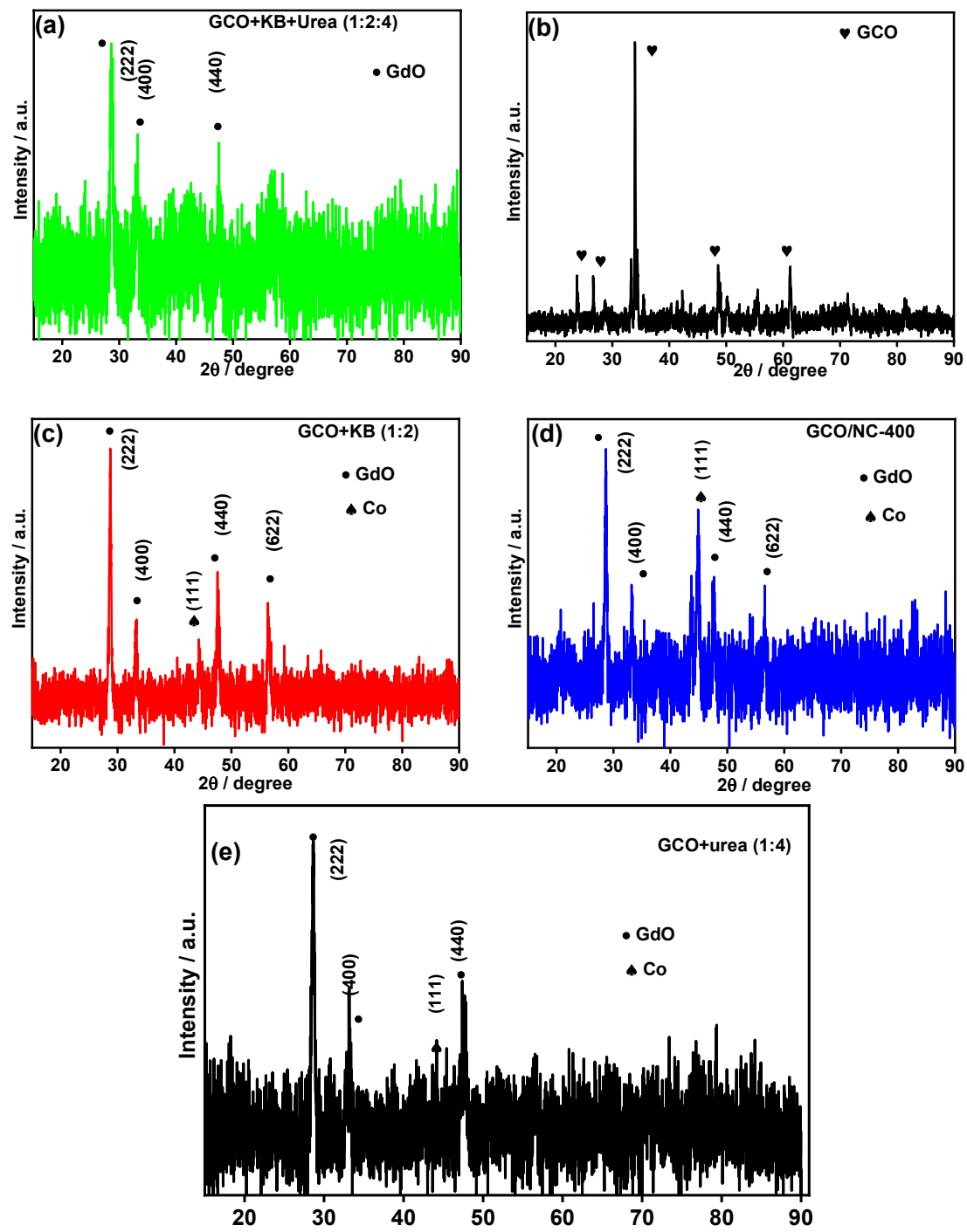


Figure S5. XRD after TGA analysis of (a) Wet ball milled GCO+ KB+ urea (1:2:4) precursor, (b) GCO, (c) wet ball milled GCO+KB (1:2), (d) and GCO/NC-400 and (e) GCO+urea (1:4) in N₂ atmosphere at 5 °C min⁻¹ as the ramp rate.

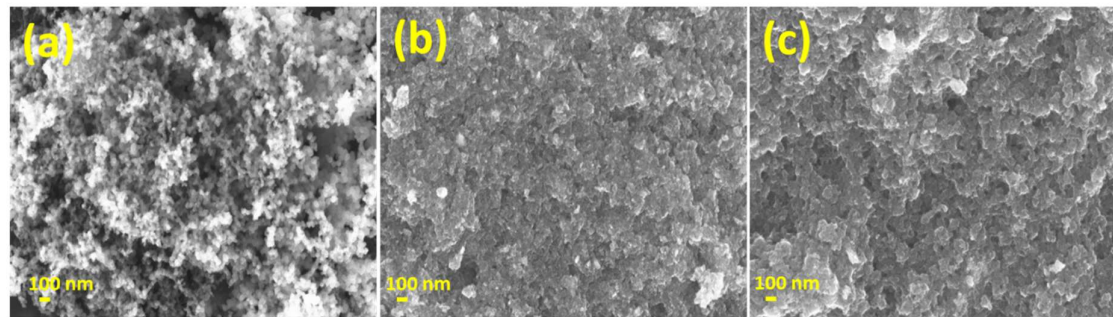


Figure S6. FE-SEM images of (a) KB, (b) GdO/NC-400 and (c) CoO/NC-400

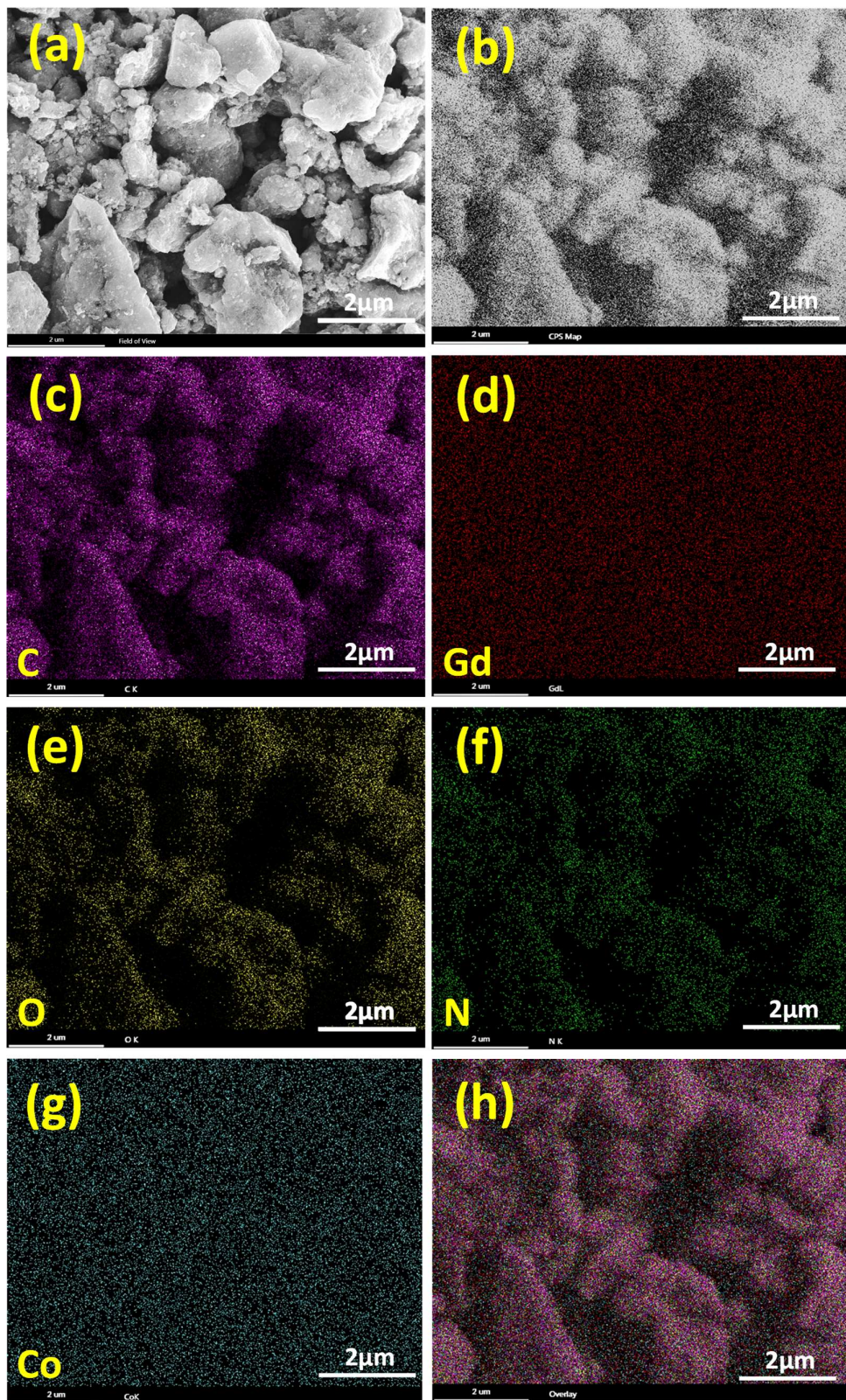


Figure S7. (a) SEM and (b) field view of GCO/NC-400 and the Elemental mapping of individual elements (c) C, (d) Gd, (e) O, (f) N, (g) Co, and (h) overlap of all the above

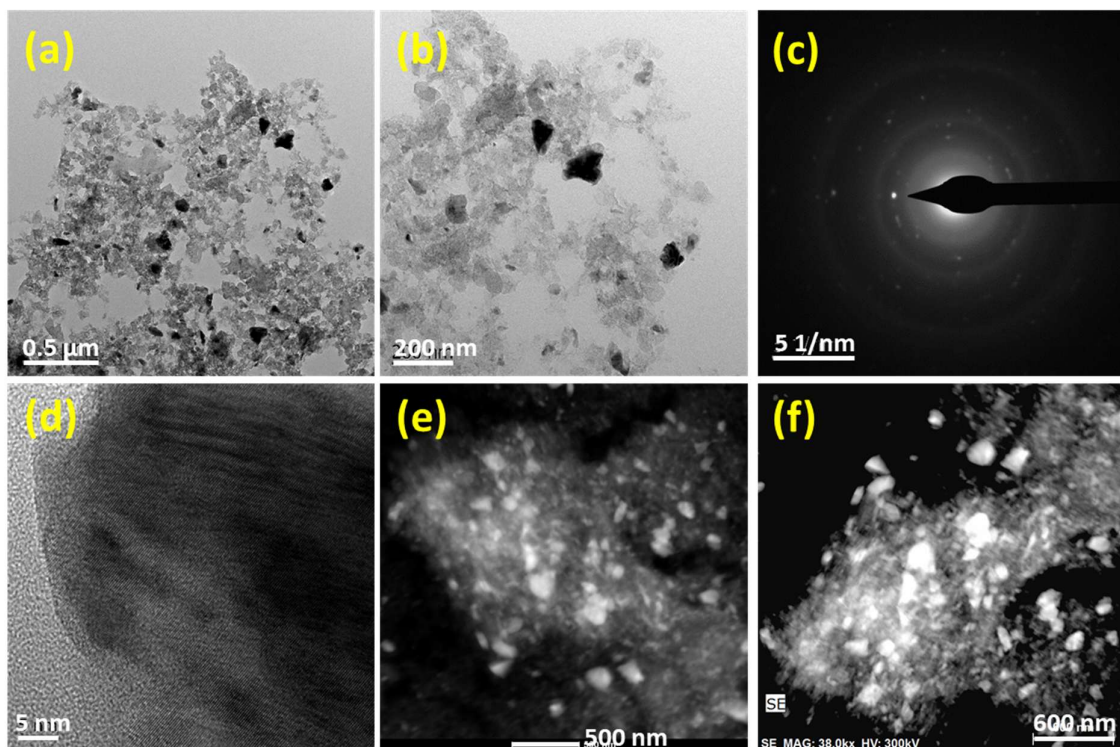


Figure S8. (a, b, d) HR-TEM images, (c) SAED patterns and (e and f) HAADF STEM images of GCO/NC-400.

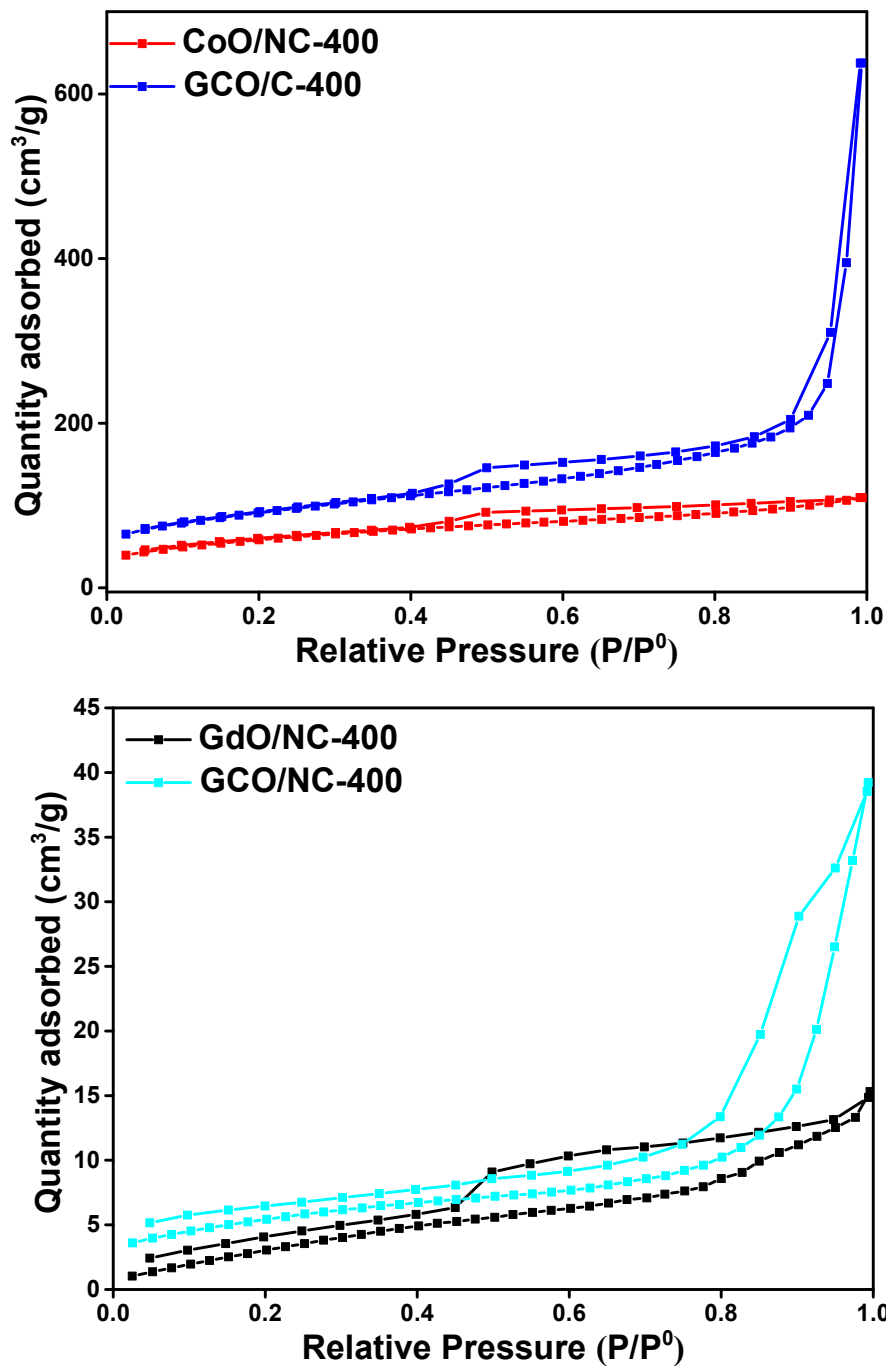


Figure S9. BET isotherms of the GCO and individual oxides N-doped carbon compounds

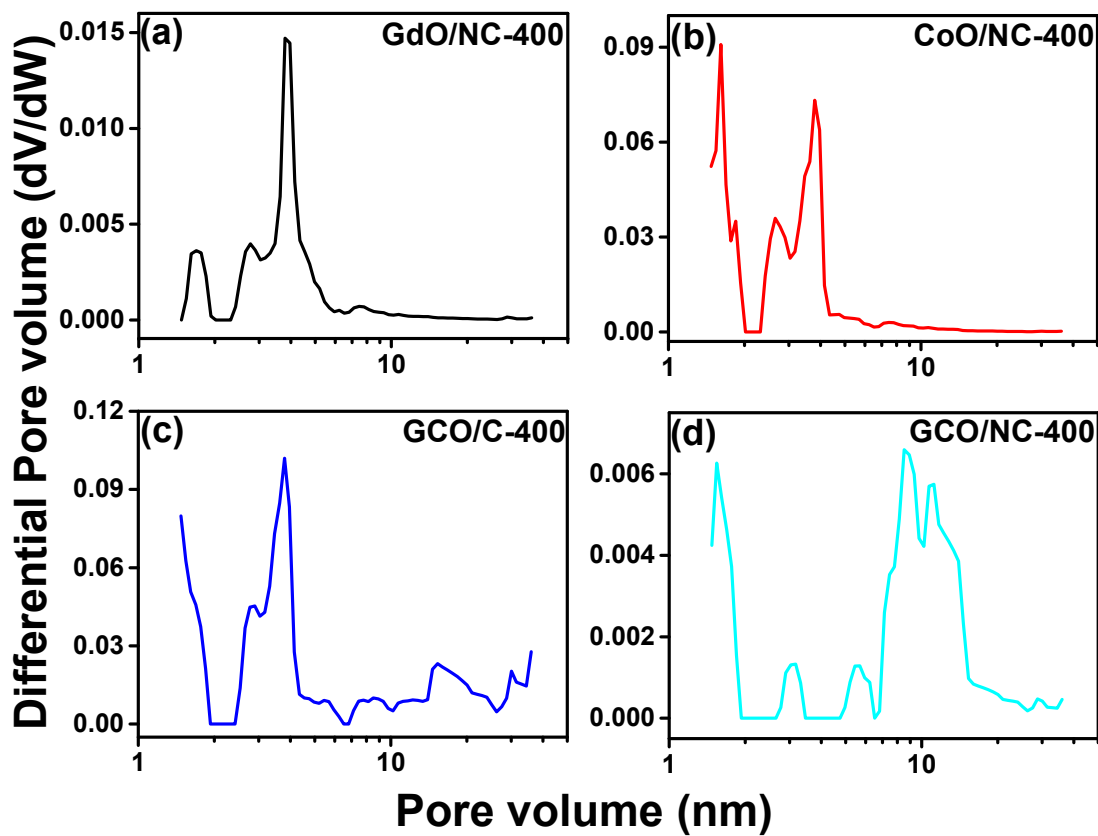


Figure S10. The pore size distribution plots from the NLDFT method of the Synthesised N-doped metal oxides.

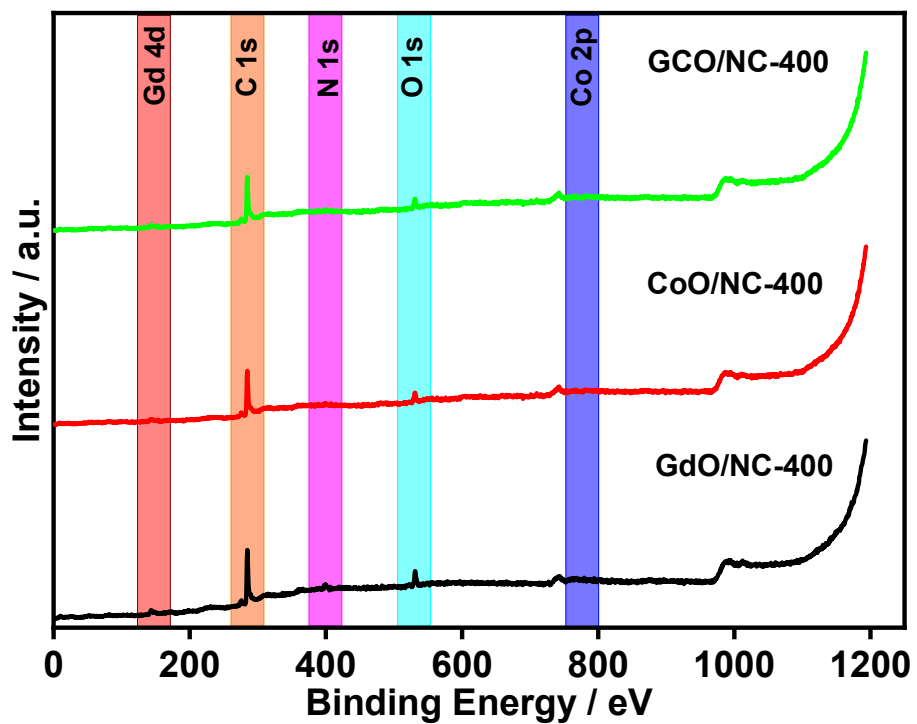


Figure S11. XPS survey spectrum of GdO/NC-400, CoO/NC-400, and GCO/NC-400

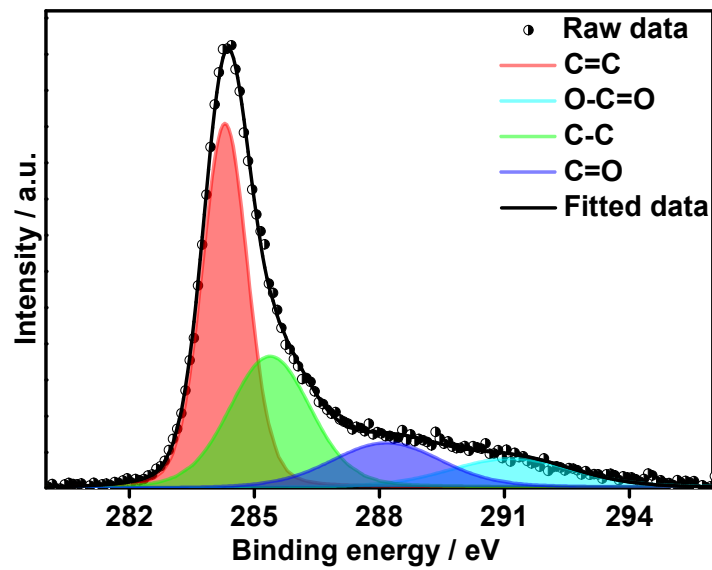


Figure S12. Deconvoluted core level C-1s XPS spectrum of GCO/NC-400

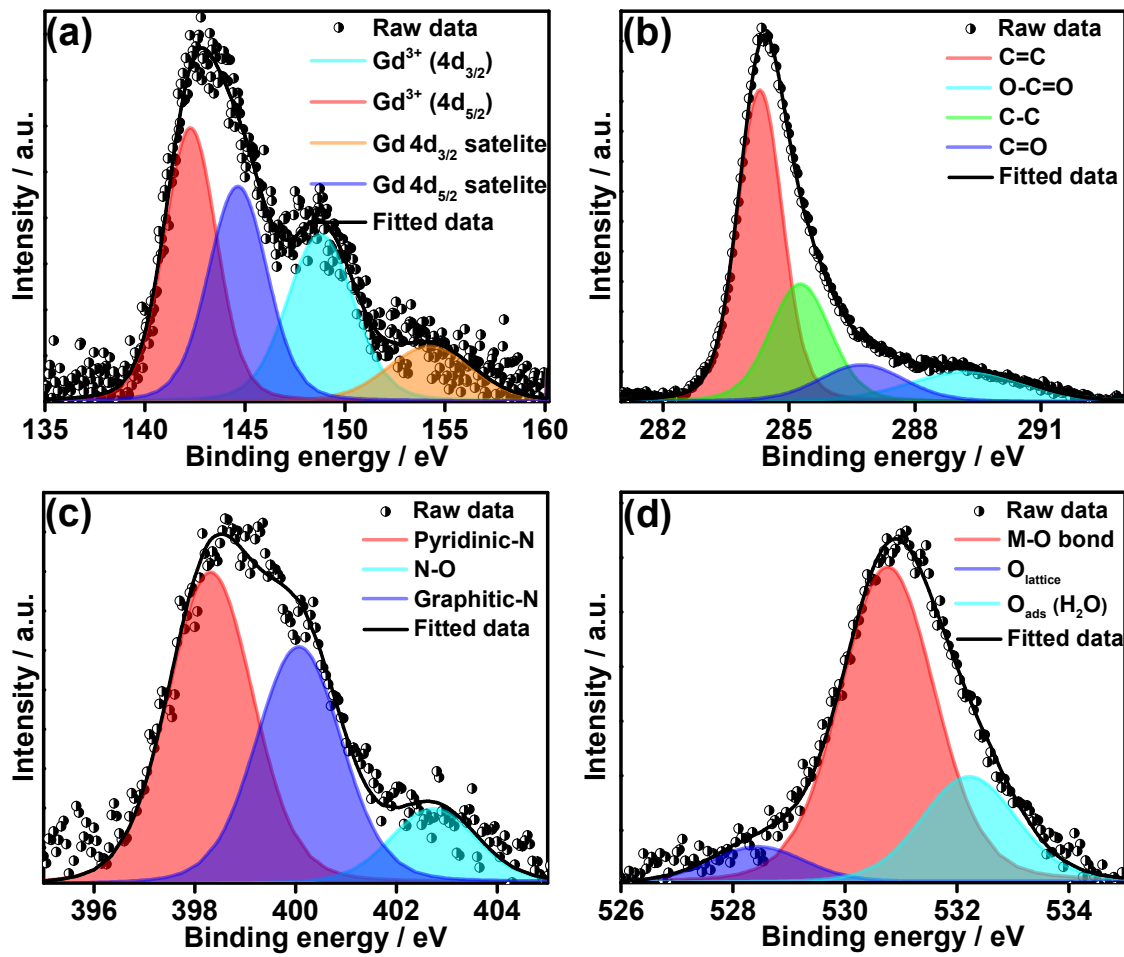


Figure S13. Deconvoluted XPS spectra of (a) Gd-4d, (b) C-1s, (c) N-1s, and (d) O-1s spectra of GdO/NC-400.

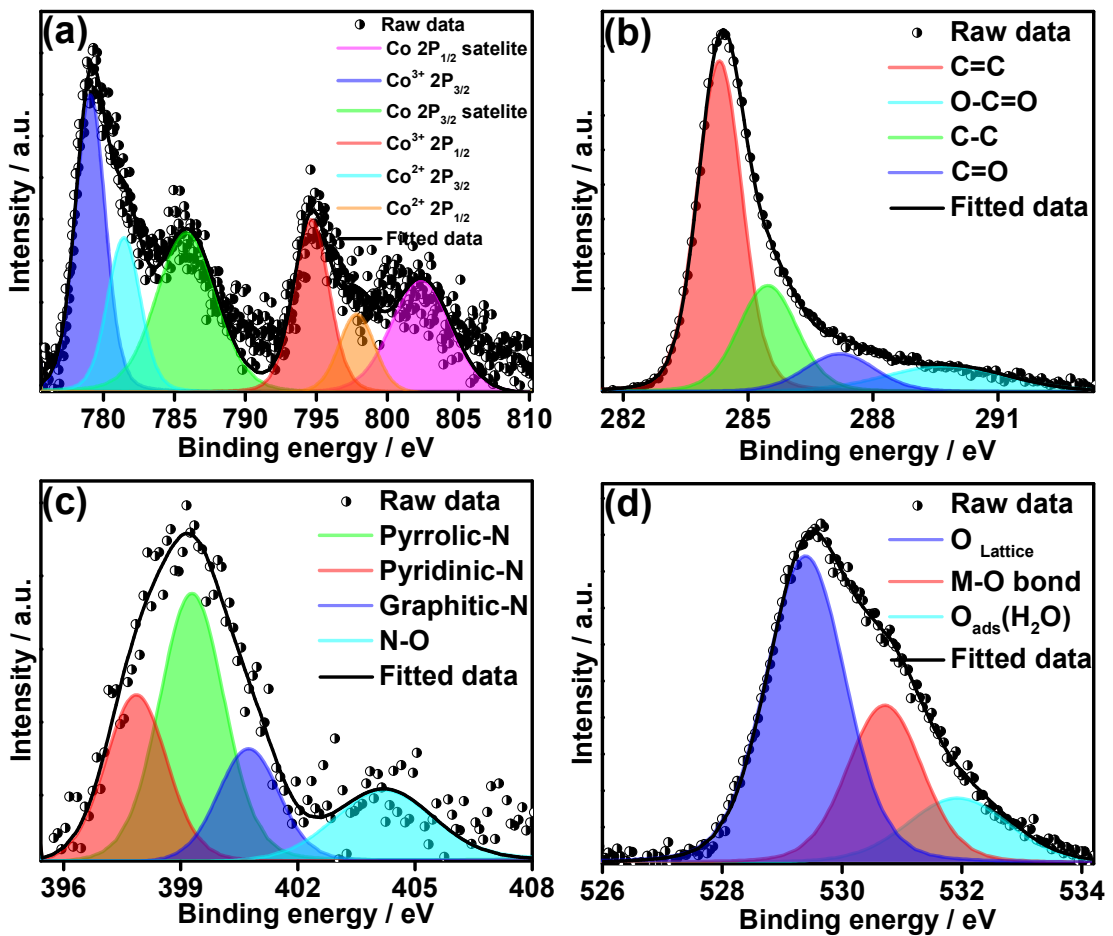


Figure S14. Deconvoluted XPS spectra of (a) Co-2p, (b) C-1s, (c) N-1s, and (d) O-1s spectra of CoO/NC-400.

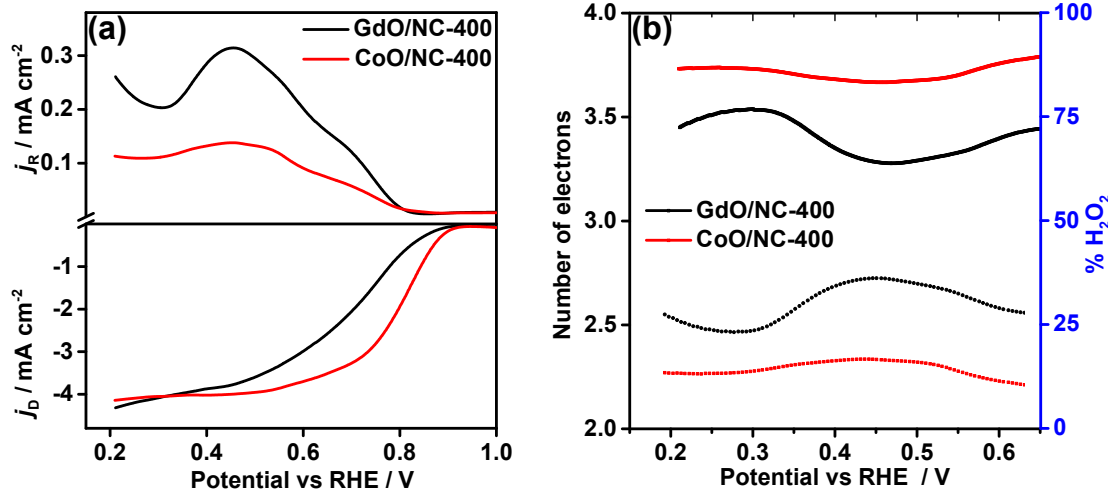


Figure S15. RRDE voltammograms of ORR of synthesised GdO/NC-400 and CoO/NC-400 at 0.1 M KOH as the electrolyte at a rotational speed of 1600 rpm in 10 mV s^{-1} as the scan rate and (b) the corresponding number of electrons and $\% \text{ H}_2\text{O}_2$.

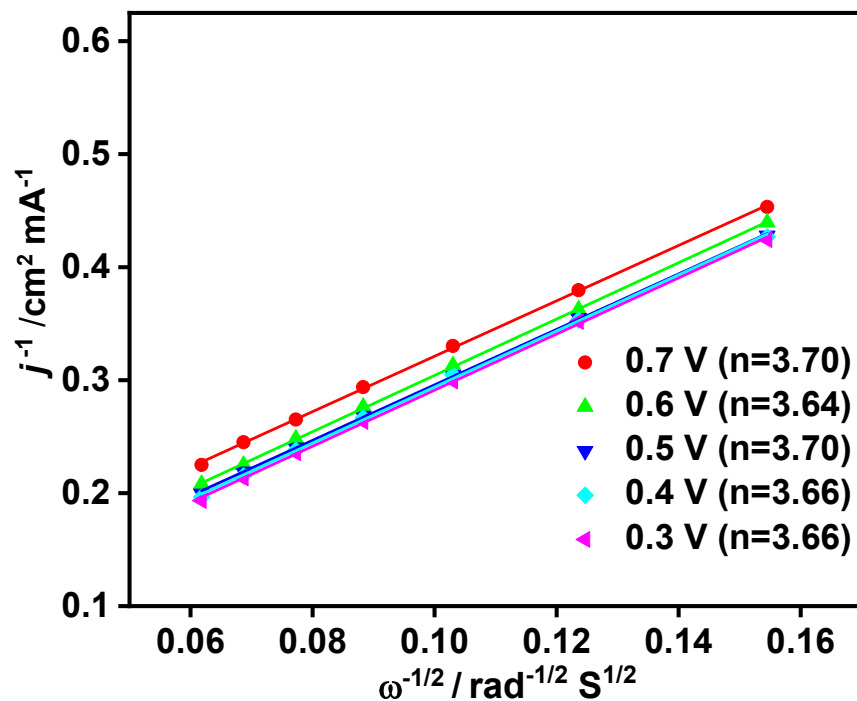


Figure S16. The Koutecky-Levich plot of the GCO/NC-400 at different applied potential. The number of electrons (n) is calculated from the slope of the K-L plot

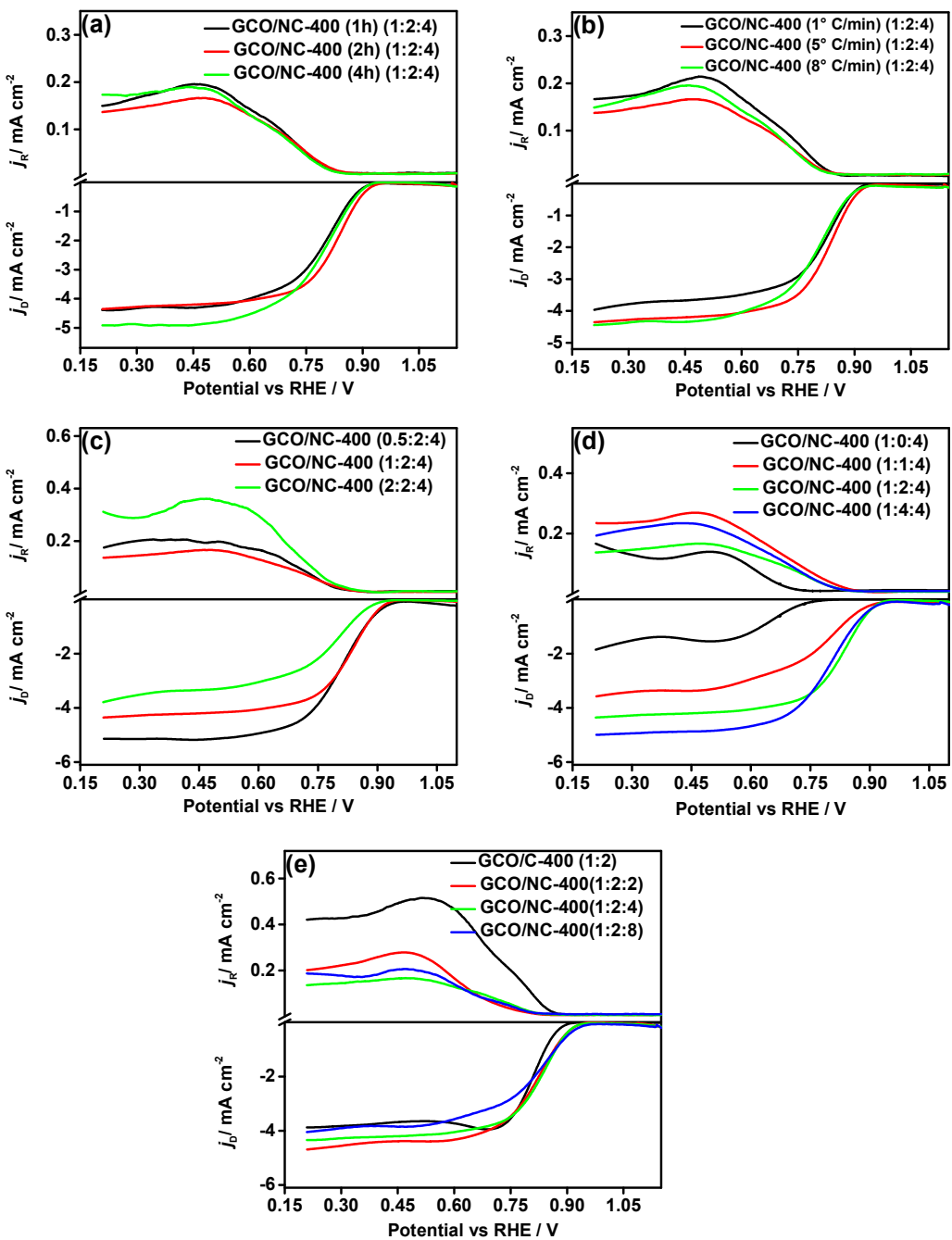


Figure S17. Optimization of the ORR activity for various (a) pyrolysis times, (b) ramp rates, (c) ratio of GCO, (d) ratios of carbon precursors, (e) ratios of nitrogen precursors. All of them pyrolysed at 400 °C.

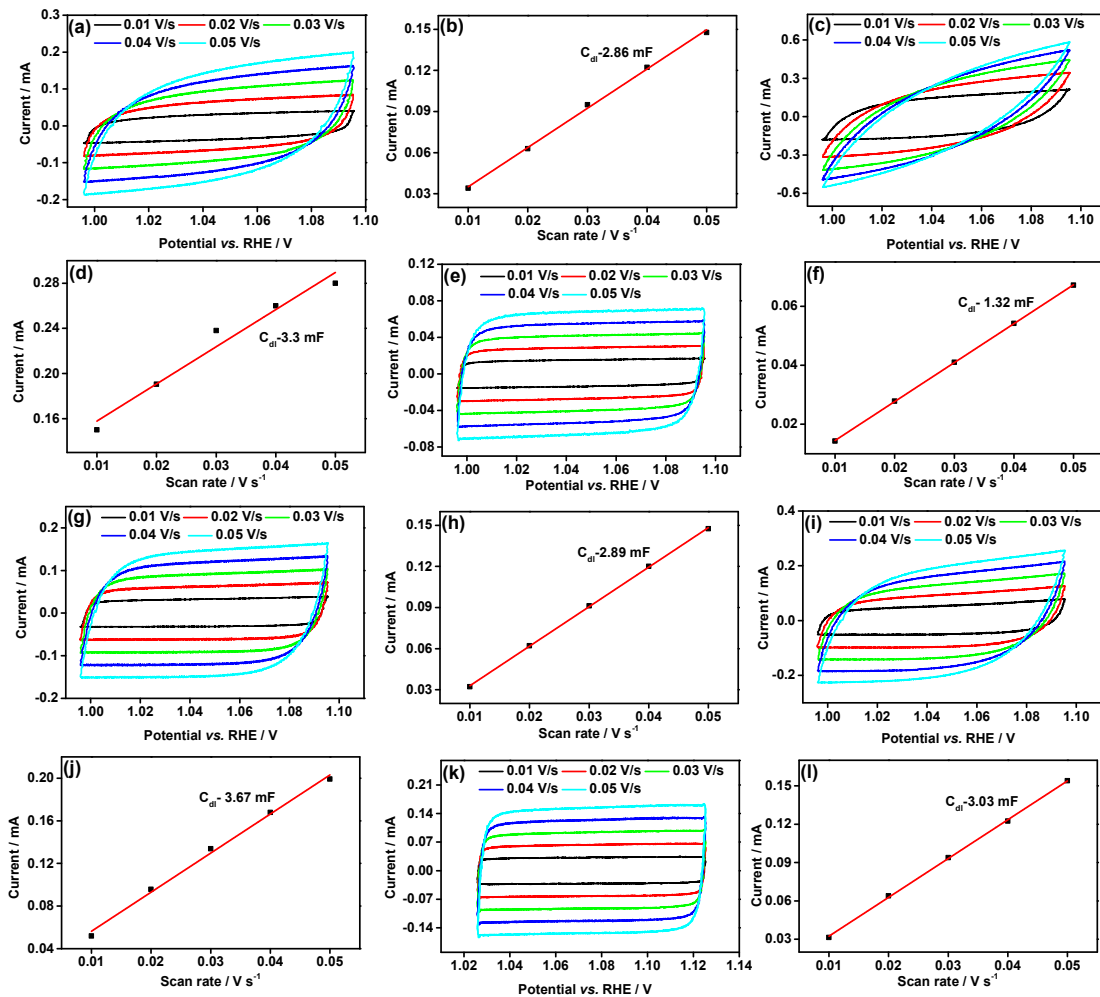


Figure S18. Cyclic voltammograms were recorded in the non-Faradaic area at different scan rates, and double-layer capacitance measurements were taken, respectively of (a) & (b) GdO/NC-400, (c) & (d) CoO/NC-400, (e) & (f) GCO+C, (g) & (h) GCO/C-400, (i) & (j) GCO/NC-400 and (k) & (l) RuO₂ in 0.1 M KOH.

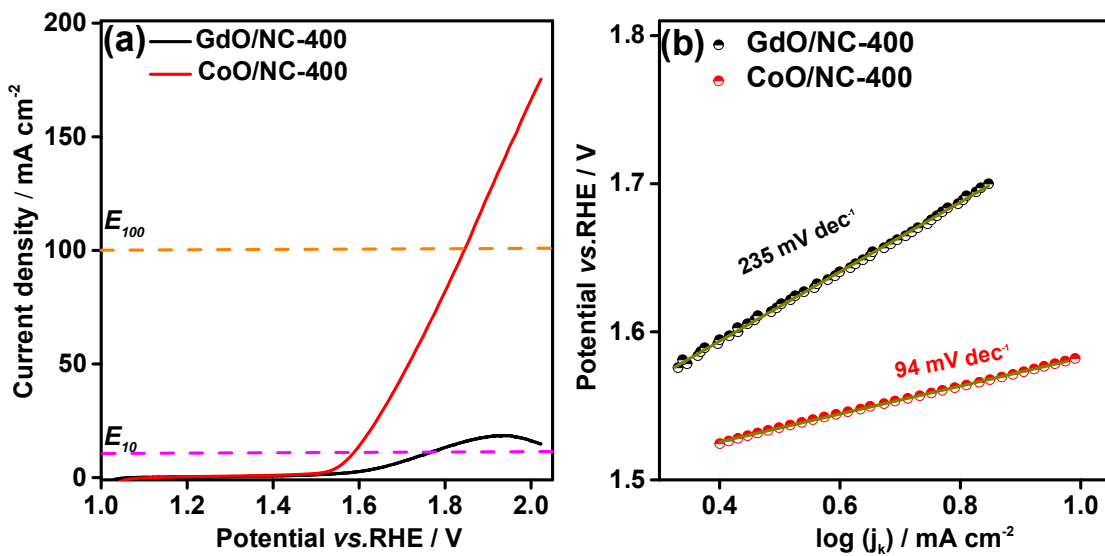


Figure S19. The linear sweep voltammograms of synthesised electrocatalysts in the OER region (1.0 to 2 V vs. RHE) in 1 M KOH as the electrolyte and at 10 mV s^{-1} as the scan rate, and the electrode was rotated at 2000 rpm, and (b) the estimated Tafel slope values.

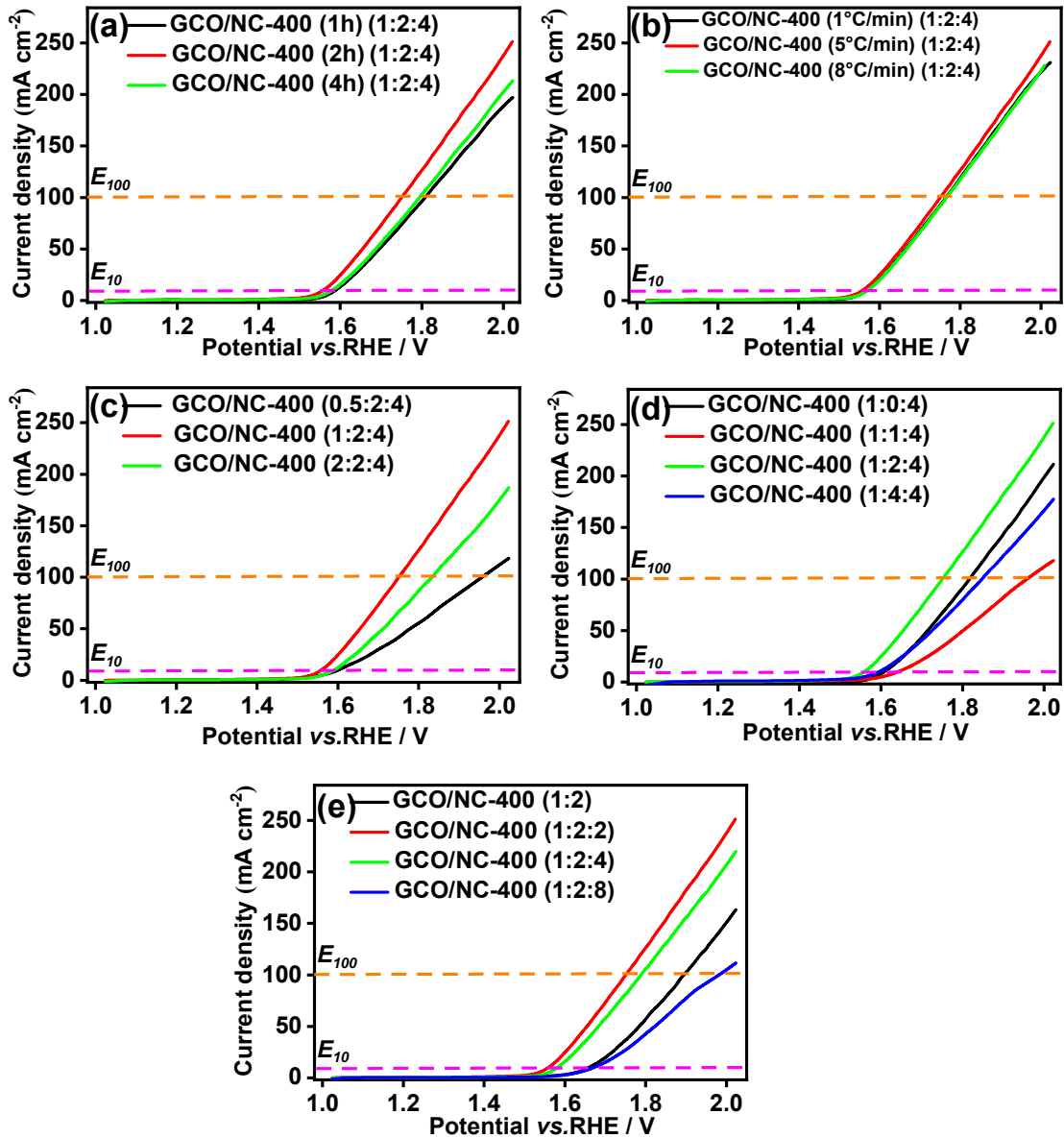


Figure S20. Optimization of the OER activity for various (a) pyrolysis times, (b) ramp rates, (c) ratios of GCO, (d) ratios of carbon precursors, (e) ratios of nitrogen precursors. All of them pyrolysed at 400 °C.

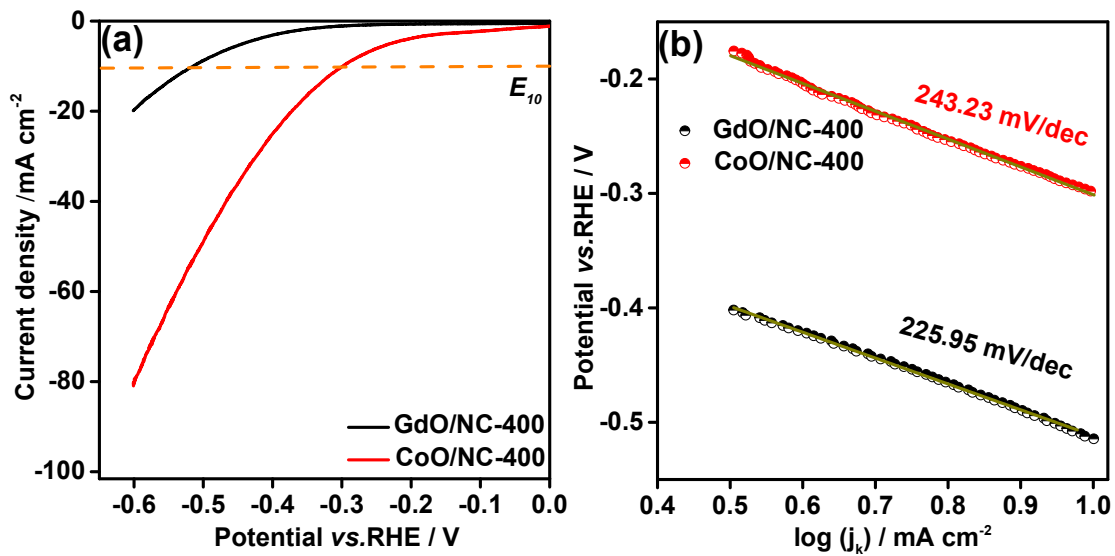


Figure S21. The linear sweep voltammograms of synthesised electrocatalysts in the HER region (0 to -0.6 V vs. RHE) in 1 M KOH as the electrolyte and at 10 mV s^{-1} as the scan rate, and the electrode was rotated at 2000 rpm, and (b) the estimated Tafel slope values.

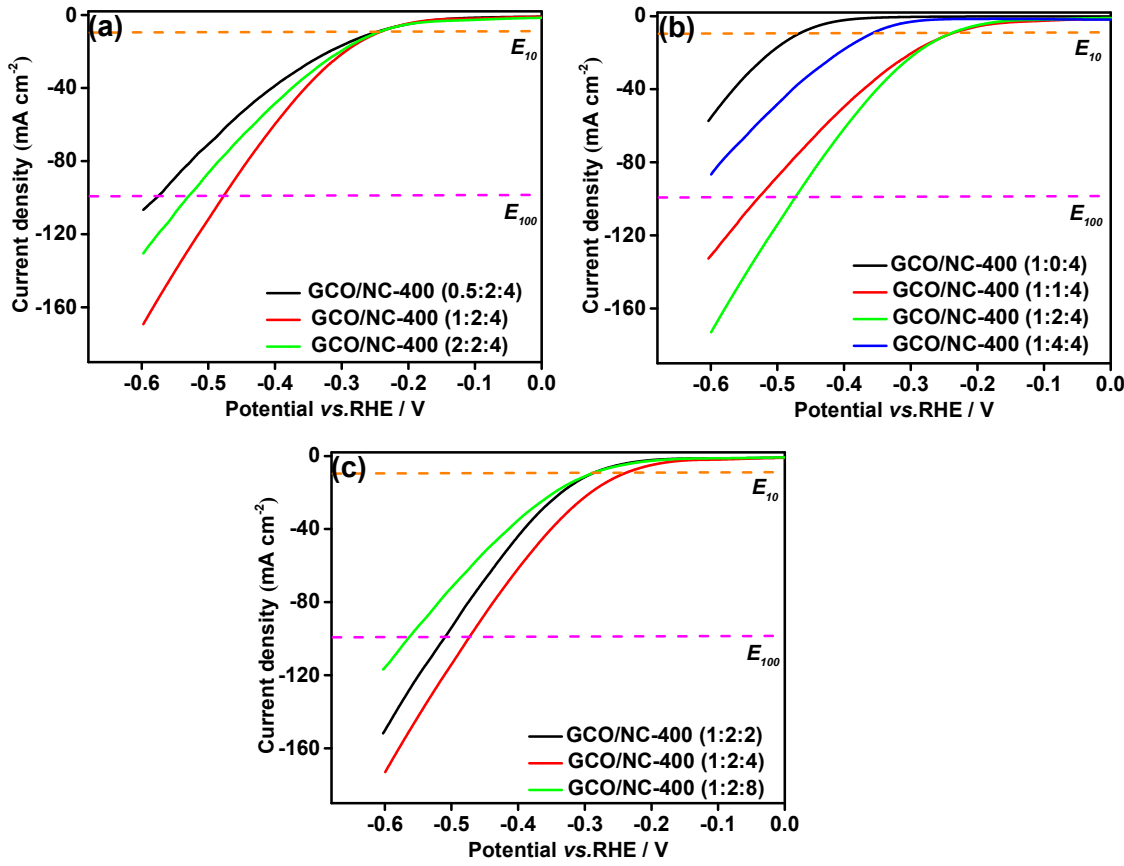


Figure S22. HER activity of the control samples by varying the weight ratios of (a) GCO in GCO: KB: Urea precursor heated in the N_2 atmosphere at $400\text{ }^\circ\text{C}$, (b) KB in GCO: KB: Urea precursor heated in the N_2 atmosphere at $400\text{ }^\circ\text{C}$, and (c) Urea in GCO: KB: Urea precursor heated in the N_2 atmosphere at $400\text{ }^\circ\text{C}$.

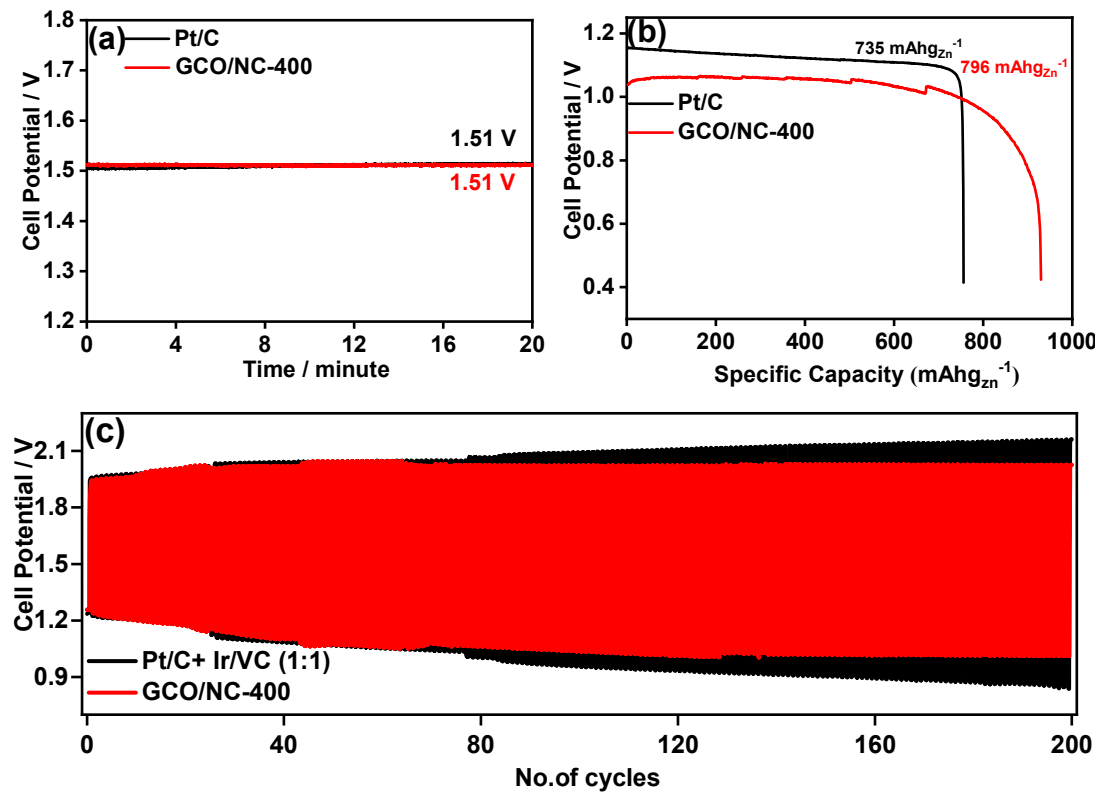


Figure S23. (a) Open circuit potential comparison of liquid electrolyte zinc-air battery constructed by GCO/NC-400 and Pt/C, (b) the specific capacity curves of the GCO/NC-400 with the benchmark Pt/C catalysts. The discharge current density is 20 mA cm^{-2} , (b) galvanostatic charge-discharge study of the GCO/NC-400 at the discharge current density of 5 mA cm^{-2} with 20 minutes per cycle.

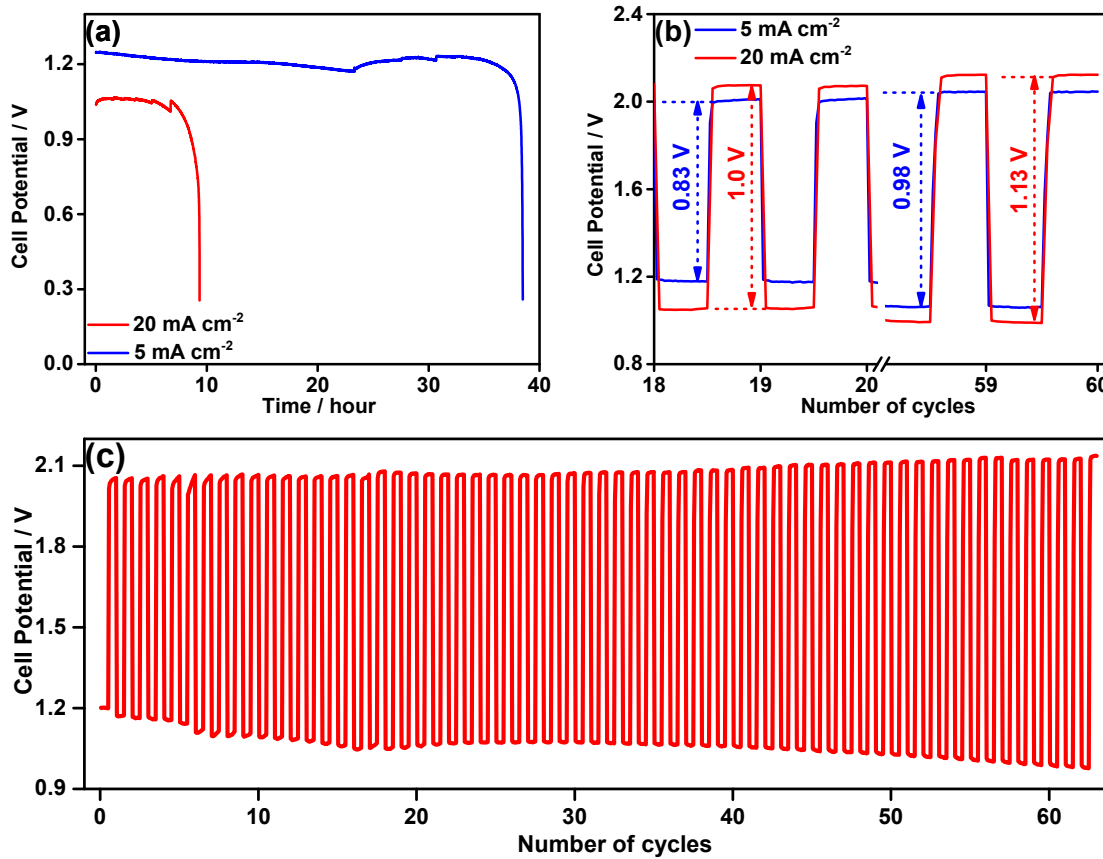


Figure S24. (a) Discharge polarization curves of GCO/NC-400 at different current densities (5 mA cm^{-2} and 20 mA cm^{-2}) (b) comparison of first and final cycles of the GCD cycles carried out at different current densities (5 mA cm^{-2} and 20 mA cm^{-2}), and (c) galvanostatic charge-discharge cycles of GCO/NC-400 catalyst at 20 mA cm^{-2} as the current density (10 min charging and 10 min discharging).

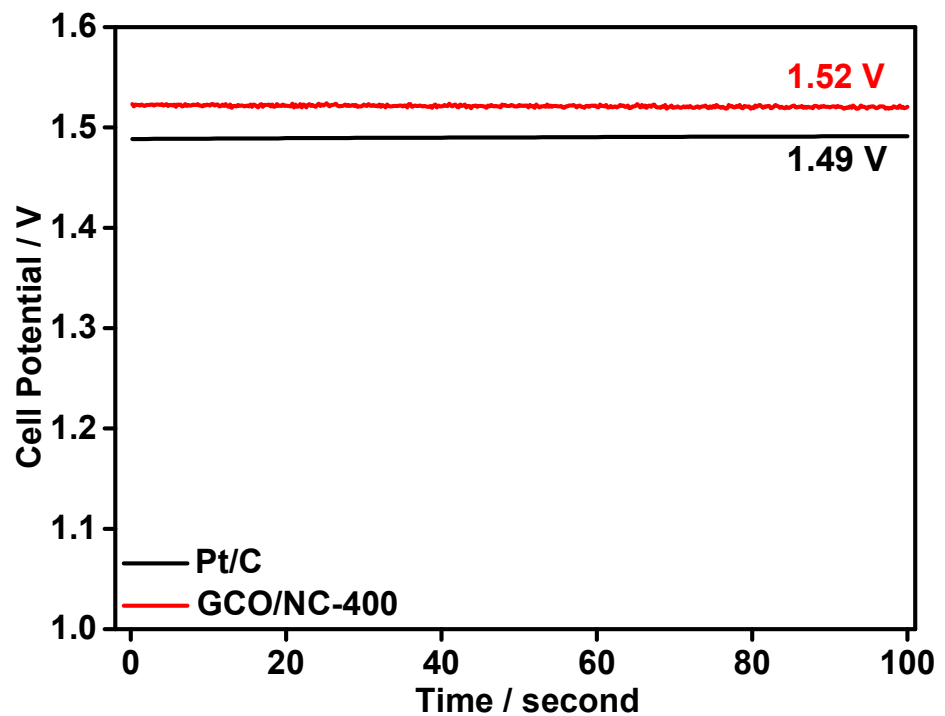


Figure S25. OCP of the solid-state zinc-air battery constructed by GCO/NC-400 and Pt/C

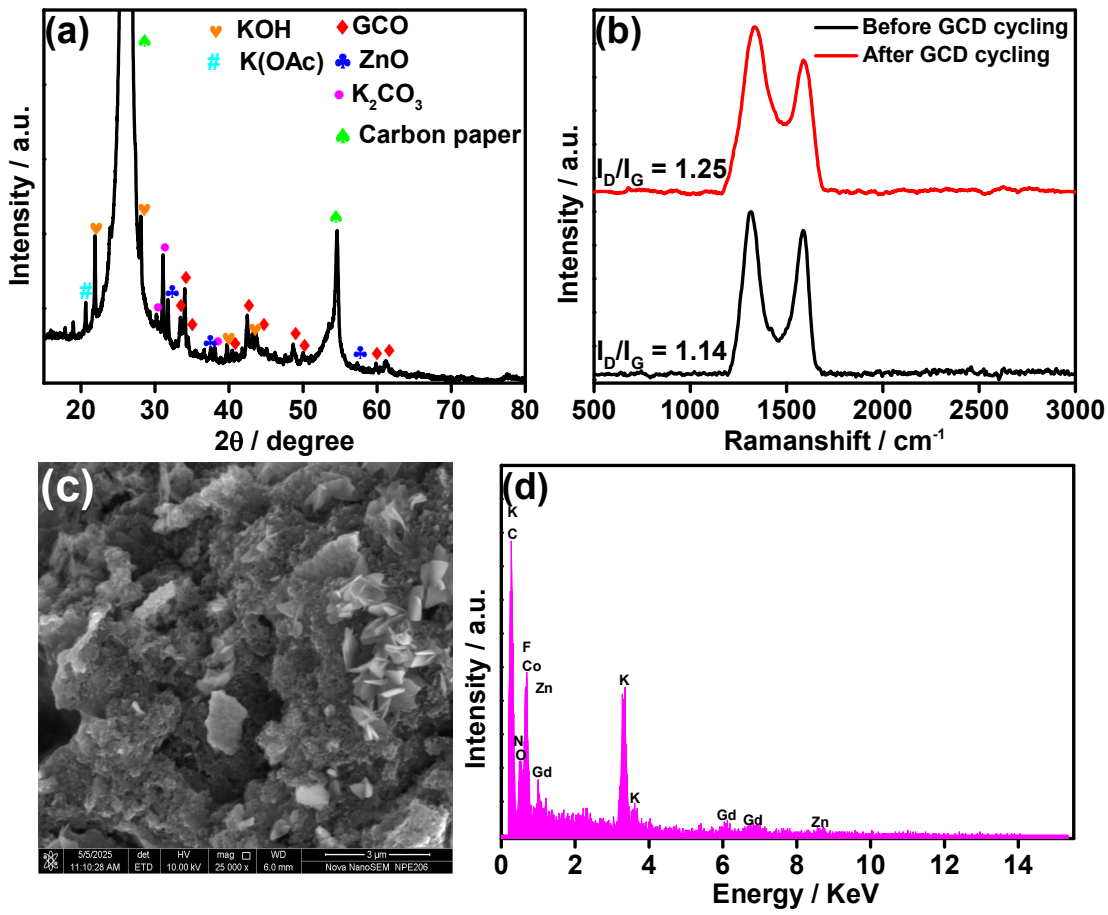


Figure S26. (a) Powder X-ray diffraction patterns, (b) Raman spectra, (c) SEM images, and (d) SEM- EDS of GCO/NC-400 after the stability test.

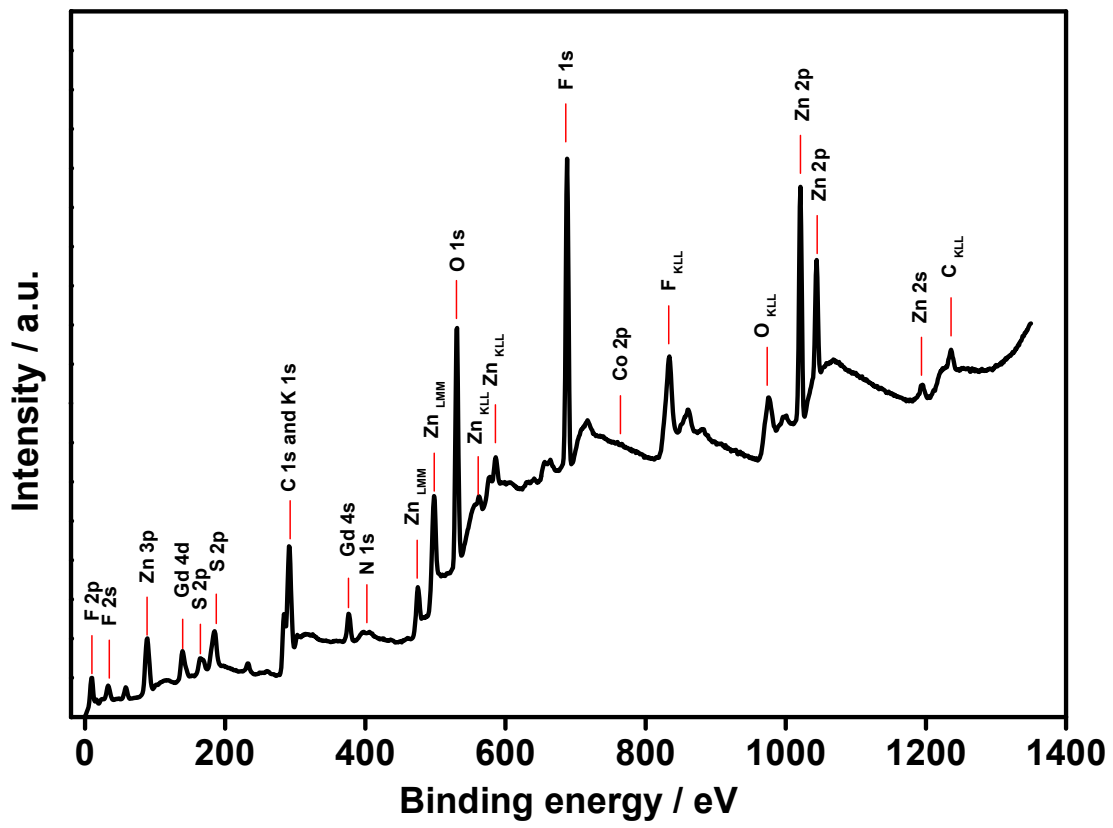


Figure S27. XPS survey spectra of GCO/NC-400 after the stability test.

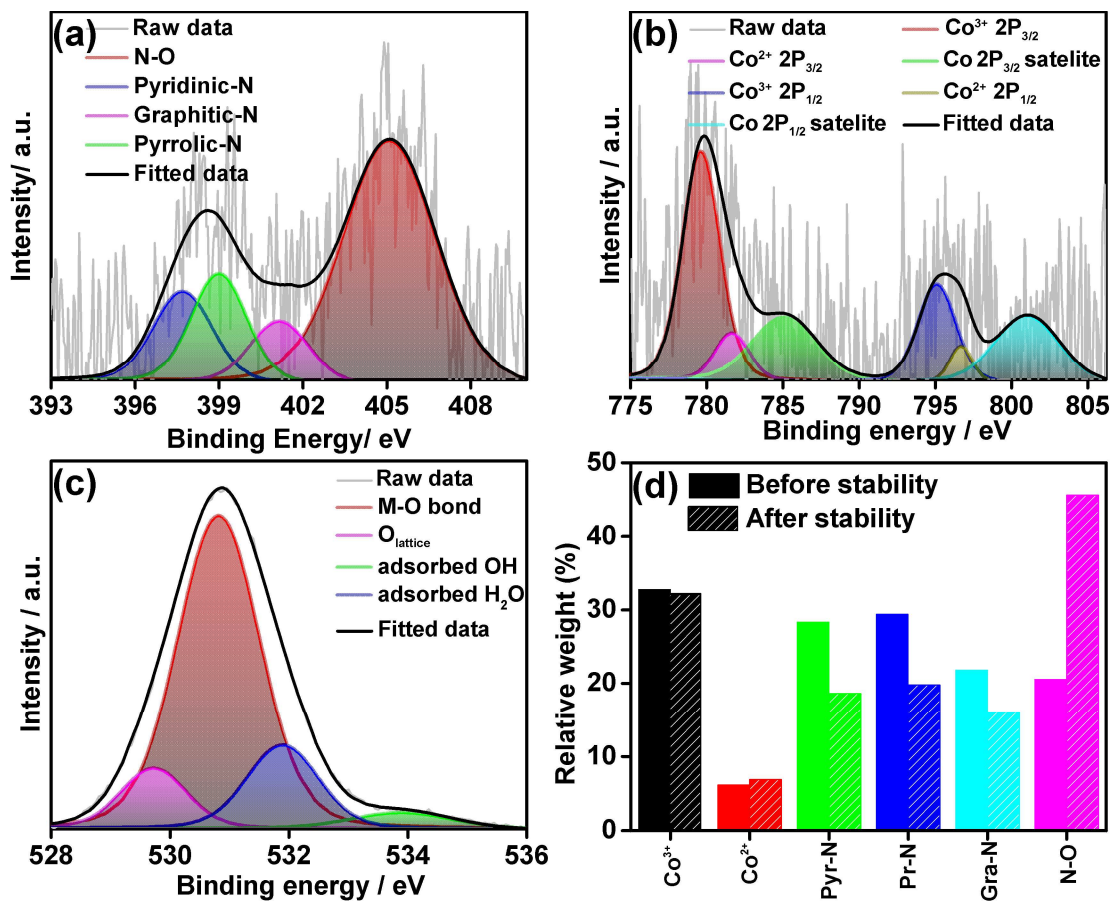


Figure S28. (a) Core level N-1s, (b) Co-2p, (c) O-1s XPS GCO/NC-400 catalysts coated on carbon paper after the 1500 GCD cycles in solid state ZAB, (d) a bar chart that contrasts the different nitrogen and cobalt species before and after the durability cycles.

Table S1. Detailed description of control samples

Optimizing Parameter – Pyrolysis temperature				
Temperature (° C)	Ratio of GCO: KB: Urea	Time (hours)	Ramp rate (°C/min)	Compound name
350	1:2:4	2	5	GCO/NC-350
400	1:2:4	2	5	GCO/NC-400
450	1:2:4	2	5	GCO/NC-450
500	1:2:4	2	5	GCO/NC-500
650	1:2:4	2	5	GCO/NC-650
800	1:2:4	2	5	GCO/NC-800
Optimizing Parameter – pyrolysis time				
400	1:2:4	1	5	GCO/NC-400 (1h)
400	1:2:4	2	5	GCO/NC-400 (2h)
400	1:2:4	4	5	GCO/NC-400 (4h)
Optimizing Parameter – ramp rate				
400	1:2:4	2	1	GCO/NC-400 (1 ° C/min)
400	1:2:4	2	5	GCO/NC-400 (5 ° C/min)
400	1:2:4	2	8	GCO/NC-400 (8 ° C/min)
Optimizing Parameter – weight ratio of GCO: KB: Urea				
400	0.5:2:4	2	5	GCO/NC-400 (0.5:2:4)
400	1:2:4	2	5	GCO/NC-400 (1:2:4)
400	2:2:4	2	5	GCO/NC-400 (2:2:4)
400	1:0:4	2	5	GCO/NC-400 (1:0:4)
400	1:1:4	2	5	GCO/NC-400 (1:1:4)
400	1:4:4	2	5	GCO/NC-400 (1:4:4)
400	1:2:0	2	5	GCO/NC-400 (1:2:0)
400	1:2:2	2	5	GCO/NC-400 (1:2:2)
400	1:2:8	2	5	GCO/NC-400 (1:2:8)

Table S2. The XRD peak positions of GdCoO_3 and its corresponding lattice planes.

Peak position (2θ)/ °	Lattice planes
23.7	(002)
26.6	(111)
33.2	(020)
33.9	(112)
34.3	(200)
35.3	(021)
40.3	(211)
41.4	(022)
42.3	(202)
43.7	(113)
48.5	(220)
48.8	(004)
50.1	(221)
55.5	(131)
59.7	(132)
60.4	(024)
61.2	(312)
66.6	(133)
71.3	(224)

Table S3. Summary of parameters obtained from BET adsorption isotherms

Compound	BET S.A. (m²/g)	Pore diameter (nm)	Pore Volume (cm³/g)
GdO/NC-400	14.69	3.79	0.02
CoO/NC-400	212.24	1.61	0.15
GCO/C-400	327.55	3.79	0.58
GCO/NC-400	20.01	8.53	0.052

Table S4. Double layer capacitance and electrochemical surface area of the materials estimated from the non-faradaic region.

Compound	C_{dl} (mF)	ECSA (cm²)
GdO/NC-400	2.86	71.5
CoO/NC-400	3.3	82.5
GCO+C	1.32	33
GCO/C-400	2.89	72.2
GCO/NC-400	3.67	91.7
RuO ₂	3.03	75.75

Table S5. A comparison table showing the $E_{1/2}$ (ORR), E_{10} (OER), and ΔE values of all the composite under study.

Catalyst	Ramp rate (° C/min)	Duration (hour)	$E_{1/2}$ (ORR)	E_{10} (OER)	ΔE
GdO/NC-400 (1:2:4)	5	2	0.69	1.75	1.06
CoO/NC-400 (1:2:4)	5	2	0.79	1.58	0.79
GCO/NC-400 (1:2:4)	5	1	0.79	1.58	0.78
GCO/NC-400 (1:2:4)	5	2	0.82	1.56	0.74
GCO/NC-400 (1:2:4)	5	4	0.79	1.58	0.78
GCO/NC-400 (1:2:4)	1	2	0.81	1.58	0.77
GCO/NC-400 (1:2:4)	5	2	0.82	1.56	0.74
GCO/NC-400 (1:2:4)	8	2	0.79	1.58	0.78
GCO/NC-400 (0.5:2:4)	5	2	0.81	1.6	0.79
GCO/NC-400 (2:2:4)	5	2	0.77	1.59	0.82
GCO/NC-400 (1:0:4)	5	2	0.63	1.61	0.98
GCO/NC-400 (1:1:4)	5	2	0.76	1.64	0.88
GCO/NC-400 (1:4:4)	5	2	0.79	1.6	0.81
GCO/NC-400 (1:2:0)	5	2	0.8	1.65	0.85
GCO/NC-400 (1:2:2)	5	2	0.81	1.59	0.78
GCO/NC-400 (1:2:8)	5	2	0.81	1.67	0.86

Table S6. Comparison table of HER activity of synthesised composites.

Catalyst	HER (overpotential(mV))
GdO/NC-400 (1:2:4)	516
CoO/NC-400 (1:2:4)	293
GCO/NC-400 (0.5:2:4)	249
GCO/NC-400 (1:2:4)	241
GCO/NC-400 (2:2:4)	245
GCO/NC-400 (1:0:4)	465
GCO/NC-400 (1:1:4)	236
GCO/NC-400 (1:4:4)	331
GCO/NC-400 (1:2:2)	290
GCO/NC-400 (1:2:8)	378

Table S7. Mass-specific ORR, OER and HER activities of synthesised materials with respect to metal oxide content.

Compound	ORR @ 0.8 V	OER @ 1.55 V	HER @ -0.25 V
	(A g_{Mo}^{-1})	(A g_{Mo}^{-1})	(A g_{Mo}^{-1})
GdO/NC-400	6.16	12.09	5.62
CoO/NC-400	25.94	31.48	42.72
GCO+C	6.76	5.66	3.03
GCO/C-400	41.30	12.11	8.48
GCO/NC-400	51.18	53.96	77.01

MO represents Metal oxide

Table S8. Turn over frequency for OER of the synthesised materials with the benchmark RuO₂ for comparison.

Compound	Area of CV curve (10⁻⁵)/ VA	$\tau \times 10^{15}$	I @ 1.55 V (mA)	TOF (s⁻¹)
RuO ₂	5.80	7.21	5.2	1.1
GdO/NC-400	2.34	2.91	0.43	0.2
CoO/NC-400	3.84	4.77	1.12	0.4
GCO+C	1.34	1.67	0.28	0.3
GCO/C-400	2.46	3.06	0.4	0.2
GCO/NC-400	3.11	3.87	1.92	0.8

Table S9. Turn over frequency for HER of the synthesised materials with the benchmark Pt/C for comparison.

Compound	Area of CV curve (10^{-5})/ VA	$\tau \times 10^{15}$	I @ -0.25 V (mA)	TOF (s⁻¹)
Pt/C*	53.3	33.1	9.42	0.9
GdO/NC-400	2.34	2.91	0.2	0.2
CoO/NC-400	3.84	4.77	1.52	1
GCO+C	1.34	1.67	0.15	0.3
GCO/C-400	2.46	3.06	0.28	0.3
GCO/NC-400	3.11	3.87	2.74	2.2

* taken at -0.1 V vs. RHE

Table S10. Comparison of the liquid and solid-state ZAB performance of the materials reported in the literature.

No.	Compound	Synthesis method	Liquid state ZAB		Solid state ZAB		Ref.
			Power density (mW cm ⁻²)	GCD stability	Power density (mW cm ⁻²)	GCD stability	
1	Ni _{0.6} Fe _{2.4} O ₄ @NC-1	100 °C, 48 h, 800 °C, 2 h, (N ₂)	187.1	299 h *	66.1	43 h #	S1
2	Co _{1.8} Fe _{0.2}	225 °C, 24 h, 600 °C, 15 h, 1000 °C	64	350 h *	-	-	S2
3	LMNO_4h	350 °C, 4 h 750 °C, 4 h, 450 °C, (NH ₃)	84	83.3 h #	-	-	S3
4	L8S2MCO/Vulcan (1:1)	500 °C, 1 h, 700 °C, 6h, (air)	44.5	20 h #	-	-	S4
5	CeO ₂ -C/PSNC	850 °C, 5 h, 400 °C, 3 h (N ₂)	161	219 h *	-	60 h @ 0.5 mA cm ⁻²	S5
6	PBSCRu@VG-5	Electrospinning, 950 °C, 5 h, 450 °C (vacuum)	242.7	200 h *	122.4	40 h #	S6
7	LMOC-50	800 °C, 3 h, 500 °C (Ar)	167	414 h #	-	-	S7
8	K0.5 -BSCF	950 °C, 5 h	98.4	150 h #	-	-	S8
9	3DOM LCCNO	200 °C, 3 h (N ₂), 450 °C, 2 h, 600 °C, 3 h (N ₂ /O ₂)	44	38 h *	-	-	S9
10	SNCF-Ni-PM	400 °C, 2 h (air), 750 °C, 2 h (N ₂)	295.9	200 h *	228.4	80 h #	S10
11	SNCF-NF-Co ₃ O ₄ @N ₂	Electrospinning, 900 °C, 2 h, 450 °C, 2 h (N ₂)	181.2	280 h *	73.3	16.7 h #	S11
12	LaMn _{0.6} Co _{0.4} O ₃ @NG	800 °C, 2 h (air), 1000 °C, 1.5 h (Ar)	101.4	1000 cycles #	-	-	S12
13	GCO/NC-400	800 °C, 3 h (air), 400 °C (N ₂)	77	66.7 h #	23.5	52.5 h @ 1 mA cm ⁻²	This work

* 10 mA cm⁻²; # 5 mA cm⁻²

References

- S1. Gopalakrishnan, M.; Kao-ian, W.; Rittiruam, M.; Praserthdam, S.; Praserthdam, P.; Limphirat, W.; Nguyen, M. T.; Yonezawa, T.; Kheawhom, S. 3D Hierarchical MOF-Derived Defect-Rich NiFe Spinel Ferrite as a Highly Efficient Electrocatalyst for Oxygen Redox Reactions in Zinc–Air Batteries. *ACS Appl. Mater. Interfaces* **2024**, *16* (9), 11537-11551.
- S2. Ozgur, C.; Erdil, T.; Geyikci, U.; Yildiz, I.; Lokcu, E.; Toparli, C. B-Site Doping Boosts the OER and ORR Performance of Double Perovskite Oxide as Air Cathode for Zinc-Air Batteries. *ChemPhysChem* **2024**, *25* (22), e202400531.
- S3. Mondal, S.; Sarkar, S.; Riyaz, M.; Kar, M.; Fortuin, A. C.; Vashishth, S.; Das, R.; Eswaramoorthy, M.; Kramer, D.; Peter, S. C. Nitrogen Doping-Induced Structural Distortion in LaMnO₃ Enhances Oxygen Reduction and Oxygen Evolution Reactions. *ACS Energy Lett.* **2024**, *9* (7), 3440-3447.
- S4. Flores-Lasluisa, J. X.; García-Rodríguez, M.; Cazorla-Amorós, D.; Morallón, E. Effect of Sr substitution in La_{1-x}Sr_xMn_{0.7}Co_{0.3}O₃ perovskites and their application in Zn-air batteries. *J. Power Sources* **2025**, *632*, 236364.
- S5. Deng, Y.; Du, J.; Zhu, Y.; Zhao, L.; Wang, H.; Gong, Y.; Jin, J.; He, B.; Wang, R. Interface engineering of Ruddlesden–Popper perovskite/CeO₂/carbon heterojunction for rechargeable zinc-air batteries. *J. Colloid Interface Sci.* **2024**, *653*, 1775-1784.
- S6. Du, J.; Zhang, N.; Zhang, W.; Shi, X.; Gong, Y.; Wang, R.; Wang, H.; Jin, J.; Zhao, L.; He, B. Synergistic Vertical Graphene-Exsolved Perovskite to Boost Reaction Kinetics for Flexible Zinc–Air Batteries. *Adv. Funct. Mater.* **2025**, *35* (7), 2415351.
- S7. Wan, K.; Li, Z.; Sun, Y.; Zhang, X.; Fang, J.; Li, Q.; Sun, Y.; Miao, H. Enhanced Catalytic Activity of LaMnO₃ Perovskite Toward Oxygen Reduction Reaction Using Oxygen-Vacancy Engineering. *ChemCatChem* **2025**, *17* (6), e202401655.
- S8. Xie, Z.; Qiu, H.; Tang, J.; Liang, Z.; He, D.; Xiao, B.; Su, C.; Shao, Z. A Potassium-Doped Perovskite-Based Nanocomposite as an Efficient Bifunctional Oxygen Electrocatalyst for Rechargeable Zn-Air Batteries. *Small* **2025**, *2502595*.
- S9. Boonlha, S.; Tirapanich, T.; Prasert, A.; Kityakarn, S.; Chakthanont, P. Enhancing the Electronic Structure of Macroporous LaCoO₃ through Ce and Ni Doping for High-Performance Bifunctional Electrocatalysts in Rechargeable Zinc–Air Batteries. *ACS Appl. Energy Mater.* **2025**, *8* (6), 3404-3415.

- S10. Zou, J.; Yuan, B.; Zhao, C.; Wang, J.; Qiu, H.; Dang, J.; Wang, Q.; Miao, H.; Yuan, J. Recycling the spent cobalt-based perovskites for the high-active oxygen catalysts in zinc-air batteries. *J. Clean. Prod.* **2024**, *462*, 142685.
- S11. Yuan, B.; Zou, J.; Jian, J.; Wang, J.; Xu, H.; Zhang, X.; Zhang, C.; Miao, H.; Yuan, J. Promoting the bifunctional oxygen catalytic activity of the perovskite and Co_3O_4 heterostructure by introducing oxygen vacancies. *Int. J. Hydrogen Energy* **2024**, *80*, 801-809.
- S12. Sun, Y.; Liu, Z.; Xiao, R.; Zhang, Y.; Yao, Z.; Han, G.; Li, J. Boosting the bifunctional electrocatalytic activity of nitrogen-doped graphene by electronic effect of heterovalent ion substituted perovskite oxides. *Int. J. Hydrogen Energy* **2024**, *51*, 904-912.